Heterodimers for in Situ Plasmonic Spectroscopy: Cu Nanoparticle Oxidation Kinetics, Kirkendall Effect, and Compensation in the Arrhenius

Citation for the original published paper (version of record):
Albinsson, D., Nilsson, S., Antosiewicz, T. et al (2019). Heterodimers for in Situ Plasmonic Spectroscopy: Cu Nanoparticle Oxidation Kinetics, Kirkendall
Effect, and Compensation in the Arrhenius Parameters. Journal of Physical Chemistry C, 123(10): 6284-6293. http://dx.doi.org/10.1021/acs.jpcc.9b00323

(article starts on next page)

Heterodimers for *in Situ* Plasmonic Spectroscopy: Cu Nanoparticle Oxidation Kinetics, Kirkendall Effect, and Compensation in the Arrhenius Parameters

David Albinsson[1], Sara Nilsson[1], Tomasz J. Antosiewicz[2], Vladimir P. Zhdanov[1,3], and Christoph Langhammer[1]*

[1]Department of Physics, Chalmers University of Technology, 412 96 Göteborg, Sweden

[2]Faculty of Physics, University of Warsaw, Pasteura 5, 02-093, Warsaw, Poland

[3]Boreskov Institute of Catalysis, Russian Academy of Sciences, Novosibirsk 630090, Russia

*clangham@chalmers.se

ABSTRACT

The ability to study oxidation, reduction, and other chemical transformations of nanoparticles in real time and under realistic conditions is a non-trivial task due to their small dimensions and the often challenging environment in terms of temperature and pressure. For scrutinizing oxidation of metal nanoparticles, visible light optical spectroscopy based on the plasmonic properties of the metal has been established as a suitable method. However, directly relying on the plasmonic resonance of metal nanoparticles as a built-in probe to track oxidation has a number of drawbacks, including the loss of optical contrast in the late oxidation stages. To address these intrinsic limitations, we present a plasmonic heterodimer-based nanospectroscopy approach, which enables continuous self-referencing by using polarized light to eliminate parasitic signals and provides large optical contrast all the way to complete oxidation. Using Au-Cu heterodimers and combining experiments with FDTD simulations we quantitatively analyze the oxidation kinetics of ca. 30 nm sized Cu nanoparticles up to complete oxidation. Taking the Kirkendall effect into account, we extract the corresponding apparent Arrhenius parameters at various extents of oxidation and find that they exhibit a significant compensation effect, implying that changes in the oxidation mechanism occur as oxidation progresses and the structure of the formed oxide evolves. In a wider perspective, our work promotes the use of model-system type *in situ* optical plasmonic spectroscopy experiments in combination with electrodynamics simulations to quantitatively analyze and mechanistically interpret oxidation of metal nanoparticles and the corresponding kinetics in demanding chemical environments, such as in heterogeneous catalysis.

Introduction

In the presence of oxygen, metals are prone to oxidation. In particular, macroscopic surfaces are usually covered by a nm-sized "native" oxide layer, preventing complete oxidation, while nanoparticles can easily be converted into the fully oxidized state. In this field, both experimental and theoretical studies of oxidation have long been focused on macroscopic samples.[1] More recently also the oxidation of nanoparticles and nanostructures has received considerable attention due to technological relevance for various areas including microelectronics and heterogeneous catalysis (see e.g. seminal articles[2–4] and more recent studies[5–10] and references therein). However, irrespective of the length scales of the samples, the understanding of the mechanistic details governing oxidation is still limited because it is typically influenced by a subtle interplay of various factors including (i) the electric field generated due to the charge located at the interface between metal and oxide, (ii) lattice strain arising due to the lattice expansion during oxide formation, (iii) evolution of the oxide structure e.g. via grain growth, (iv) grain boundaries, and (v) generation of voids in the metal (Kirkendall effect[2,6]) and/or cracks in the oxide (see e.g. [10] and references therein).

Experimentally, the oxidation of metal nanoparticles has been explored by a wide range of techniques, including quartz crystal microbalance (QCM),[11] *in situ* X-ray diffraction (XRD),[3] thermogravimetry (TG),[12,13] UV-vis spectroscopy,[9,14–16] X-ray photoelectron spectroscopy (XPS)[11] and transmission electron microscopy (TEM).[17,18] Despite the apparent abundance of different techniques, the accurate monitoring of oxidation is still challenging because each of them has its limitations. For example, techniques relying on high-energy electrons (TEM, XPS) to probe or image a sample suffer from the need of low operation pressures and tend to significantly influence the oxidation process during (beam effects) as well as after imaging (due to carbon contamination build-up), while gravimetric techniques (QCM, TG) require relatively large samples and lack spatial resolution. Among the above mentioned approaches,

visible light optical spectroscopy, and plasmonic spectroscopy in particular, is attractive because of its remote readout compatible with ambient pressures and elevated temperatures, combined with its generally non-invasive nature due to the low irradiance of the employed visible photons.

In general, plasmonic spectroscopy relies on measuring the spectral characteristics of the localized surface plasmon resonance (LSPR) peak of (typically) metallic nanoparticles, and how it responds due to changes in and around the particle(s). This effect gives rise to a large and conveniently measurable optical contrast upon oxide formation because the LSPR frequency changes with the transition from the metallic state supporting LSPR to a dielectric state that is plasmonically inactive and thus exhibits a much smaller optical cross section. Nevertheless, relying entirely on the intrinsic LSPR of the metallic nanoparticles as a probe of oxidation has a number of drawbacks. First, the essentially complete loss of well-defined optical contrast in the later stages of the oxidation process, when most of the metal has been converted to the oxide phase, makes its study challenging using LSPR. Secondly, along the same lines, also the study of small particles is less effective due to their smaller optical cross sections. Finally, the change in the LSPR is not selectively sensitive to the oxidation process alone, but also to other potentially simultaneously occurring effects like temperature change,[19,20] desorption of species from the nanoparticle/oxide surface[21] and chemical/dielectric changes occurring in the support.[22] To address these limitations, we apply here a plasmonic heterodimer based nanospectroscopy approach, which enables continuous self-referencing by using polarized light to eliminate unwanted signal contributions and drift,[23] and provides high optical contrast all the way to complete oxidation.

Focusing on the oxidation of Cu, we note that this process is generic in the field under consideration and that Cu exhibits excellent plasmonic properties.[24] Mechanistically the oxidation is usually considered to be controlled primarily by diffusion of Cu^+ towards the

oxide-gas interface and partly by diffusion of O^{2-}-species towards the oxide-metal interface.[1] In macroscopic, polycrystalline samples, with increasing temperature (from 200 to 700 K), the oxide thickness has been reported to increase from ~10 to 1000 nm, and the corresponding kinetics were observed to follow logarithmic, inverse-logarithmic, cubic, linear, and parabolic laws.[25] In the case of single-crystal (111), (100) and (110) surfaces, with increasing temperature from 300 to 450 K, the oxide film thickness was measured to increase from a few nm to ~100 nm, and the oxide growth was logarithmic for thicknesses under 5 nm and of the power law type with exponents of 1/3 and 1/2 in the range of 5 – 25 nm and above 25 nm, respectively.[26] Furthermore, the available oxidation studies focused on Cu nanoparticles indicate that they, in analogy with other metals,[2,6,27,28] often exhibit the so-called nanoscale Kirkendall effect (NKE), as a result of Cu-ions diffusing faster in the oxide compared to O-ions.[4,9,14,29,30] This results in the formation of a characteristic hollow oxide shell, with the amount of hollowing depending on the ratio between the diffusion rates of Cu- and O-ions, as well as on the oxide structure.

In nanoparticles at relatively low temperatures, in analogy with bulk systems, preferential formation of Cu_2O (over CuO) is typically observed[9,12,13] and the reported activation energies cover a wide range.[9,12,14] In the corresponding studies, the measured oxidation kinetics are typically explained by assuming a single set of Arrhenius parameters and to the best of our knowledge no one has investigated the correctness of this assumption or quantified the change of these parameters with increasing extent of oxidation. Hence, in this study we utilize the plasmonic heterodimer concept to track the oxidation of ~30 nm sized Cu nanoparticles all the way to complete oxidation. We observe NKE from transmission electron microscope (TEM) images and by combining optical experiments with finite-difference time-domain (FDTD) simulations, we find that the Arrhenius parameters for oxidation

significantly depend on the extent of oxidation and exhibit a distinct compensation effect between the apparent activation energy and the pre-exponential factor.

Methods

Au-Cu Heterodimer Nanofabrication

To make the structures, a hole-mask with 100 nm circular holes was prepared.[31] As the first deposition step to grow the heterodimers, 40 nm Au was electron-beam evaporated through the mask at a 2.5° angle off-normal. As the second step a 5 nm Al_2O_3 layer was evaporated through the mask at normal incidence. To then shrink the holes in the mask to tune the size of the Cu nanoparticles to be grown in the last step, the sample was tilted by 40° and 100 nm Al_2O_3 was evaporated while rotating the sample at 5 rpm. In this way, according to the SHCL concept, the evaporated Al_2O_3 is exclusively deposited on the walls of the mask without being deposited on the substrate, enabling it to be removed completely in the final lift-off. In the next step, 20 nm Cu was deposited through the same holes in the mask (now shrunk to diameters of ca. 30 nm) at an angle of 8° off normal and in the opposite direction to the Au deposition. In the last step, mask and all other material layers were removed by lift-off in acetone. All evaporations were performed at a rate of 2 Å/s and chamber base pressure of 5×10^{-7} Torr.

LSPR Measurements in Flow Reactor

Glass samples were mounted in a temperature-controlled quartz tube flow reactor with optical access (Insplorion X1, Insplorion AB, Göteborg Sweden), using Ar as the carrier gas. The gas flow rate was kept constant at 100 mL min^{-1}, and the gas composition was regulated by mass flow controllers (Bronkhorst ΔP). The sample temperature was measured by a

thermocouple mounted on the sample surface, and a PID controller (Eurotherm 3216) connected to a power supply was used to heat a coil surrounding the tube reactor. The sample inside the flow reactor was illuminated by white light (AvaLight-Hal, Avantes) through an optical fiber equipped with a collimating lens. To enable simultaneous probing of the heterodimer with light polarized along and perpendicular to its long axis, a polarizing beam splitter (Thorlabs CM1-PBS251) was placed between the sample and two fiber-coupled fixed-grating spectrometers (AvaSpec-1024, Avantes).

FDTD Simulations

The finite-difference time-domain (FDTD) simulations, performed using the commercial software FDTD Solutions (Lumerical), was used to evaluate the optical response of the plasmonic heterodimer structure. The Au sensor element in the dimer was simulated as truncated cone (81 nm bottom diameter, 66 nm top diameter and 42 nm thickness) with rounded corners (r = 20 nm top and r = 2 nm bottom). The neighboring Cu particle was simulated as a half sphere with an original radius of 22 nm placed 8 nm from the Au element. The substrate was simulated as SiO_2 (refractive index of 1.46) and the surrounding gas as a material with refractive index n=1. The Au dielectric function was taken from Johnson and Christy[31], the one for Cu from McPeak et. al.[32] and the one for Cu_2O from Tahir et. al[33]. For the various porous Cu cores, the dielectric functions were calculated using Eq. (S1). To correctly resolve the field close to the Cu particle a mesh overlay with a step size of 0.3 nm was used around it. Light was introduced as a linearly polarized plane wave via a total-field/scattered-field source and the scattering and absorption spectra were collected in all directions by integrating the Poynting vector of the field.

Results and Discussion

Au-Cu Heterodimer Nanostructures

Au-Cu heterodimer arrays were fabricated on a 1 cm^2 glass substrate using shrinking-hole colloidal lithography (SHCL)[34,35] by growing a ca. 30 x 20 nm Cu nanoparticle next to a larger Au disk nanoantenna (100 x 40 nm) acting as the sensor. The gap between the two was defined by a 5 nm thin Al_2O_3 layer grown in between the dimer elements to inhibit alloy formation between Au and Cu during heating (see Methods section for details). Scanning electron microscopy (SEM) images of the structures are presented in **Figure 1b** together with the Cu particle size distribution measured from the SEM images (**Figure 1c**). Higher resolution images (**Figure 2c,d**) indicate that initially there are tiny Au particles near the Au nanoantennas, which then almost completely disappear after heating the sample, most likely by coalescing with the large nanoantenna.

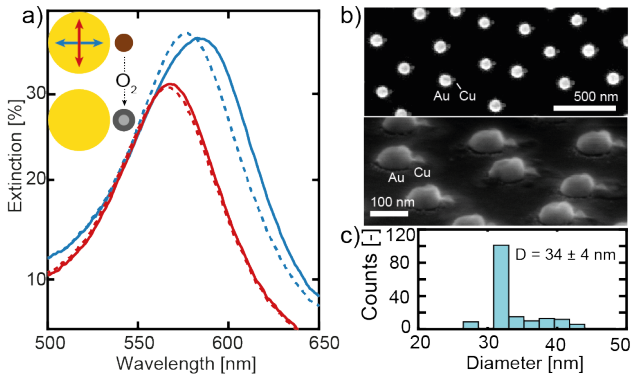

Figure 1. *a) Polarization-dependent optical extinction spectra of a heterodimer array with the Cu nanoparticles in the metallic (solid lines) and oxidized (dashed lines) state, respectively. The color code indicates the linear polarization direction with respect to the dimer axis, as depicted in the inset. Note the essentially identical optical signature for perpendicular polarization, whereas a spectral blue shift occurs upon Cu oxidation for the parallel polarization. The inset shows a schematic depiction of the Au-Cu heterodimer arrangement comprised of a Au nanoantenna sensor adjacent to a much smaller Cu nanoparticle that is oxidized upon exposure to O_2. The red and blue arrows indicate the*

simultaneously used perpendicular linear polarization directions for drift-free optical sensing of the Cu oxidation process by means of a beam splitter. b) Top-view and side-view SEM images of a nanofabricated Au-Cu heterodimer array. c) Size distribution of the Cu nanoparticles from SEM image analysis. A total of 169 particles were analyzed.

Cu Oxidation Experiments

To induce and study the oxidation of the Cu nanoparticles under controlled conditions, the heterodimer array samples were mounted in a temperature-controlled quartz tube flow reactor with optical access. Simultaneous probing of the heterodimers with light polarized along and perpendicular to its long axis was enabled by a polarizing beam splitter (Thorlabs CM1-PBS251) that was placed between the sample and two fiber-coupled fixed-grating spectrometers (AvaSpec-1024, Avantes). The observed spectral red shift, as well as the broadening of the LSPR extinction peak for the dimers excited in parallel polarization, are a clear indication of the anticipated near-field coupling between the dimer elements[36] (**Figure 1a**).

With exposing the sample to 0.2 % oxygen at 523 K to induce Cu nanoparticle oxidation (the Au remains metallic due to its chemical inertness at these conditions[37]), a significant spectral blue shift of the LSPR peak becomes apparent for the parallel polarization (blue dashed line in **Figure 1a**), while the perpendicular polarization peak is almost unchanged (red dashed line). This can be understood as plasmonic coupling and when both dimer elements are metallic,[38,39] and as the coupling diminishing when the Cu element is transformed into oxide. At the same time, any isotropic changes taking place on the Au element or in the underlying substrate will be captured in both polarization directions

symmetrically, enabling effective correction for such unwanted (symmetric) effects by subtraction of the signals obtained for the two polarization directions.[23]

To illustrate this in the present case, we carried out an experiment where a heterodimer sample was exposed to seven consecutive heating ramps from 323 K to 523 K at a heating rate of 5 K/min in increasing O_2 concentration (0.2 - 2 %) for each cycle. Ar was used as the carrier gas and prior to the first oxidation cycle, the sample was heated to 576 K in 4% H_2 in Ar for 60 min to reduce any native oxide on the Cu surface, as well as to induce Au and Cu recrystallization. This is necessary since, directly after nanofabrication, evaporated nanoparticles exhibit structure far from thermodynamic equilibrium.[32,40] After each oxidation cycle the sample was reduced in 4 % H_2 in Ar at 523 K for 60 min while cooling back to room temperature (**Figure 2a,b**). The induced LSPR centroid shift for both polarization directions, $\Delta\lambda_{cent.}$, was obtained by fitting a 20 degree polynomial to the LSPR peak in the measured optical extinction spectra for the two polarization directions and by then deriving the spectral position of the peak centroid.[41]

In addition to the contribution related to oxidation of Cu nanoparticles, the observed LSPR signal may be influenced by other factors. First, upon heating we observe a spectral red shift that is proportional to the temperature change in both polarizations. This is caused by the intrinsic temperature dependence of the LSPR.[19] Secondly, there is a parasitic signal stemming most likely from substrate effects via spill-over of e.g. H-species to the glass (SiO_2) support,[22] occurring when the surrounding atmosphere is changed from oxidizing to reducing at high temperature, as manifested in a distinct and almost immediate $\Delta\lambda$ blue shift upon exposure to H_2 for each cycle at 523 K. Thirdly, we also notice a more long-term and irreversible drift occurring over the course of the entire experiment, which gradually red shifts the LSPR peaks for both polarization directions. These can be ascribed to slow morphological changes such as recrystallization, transformation to more Wulff-shape

crystals[42] and Ostwald ripening. By inspecting SEM images taken before and after exposing a sample to elevated temperatures (**Figure 2 c,d**, respectively), one can clearly see a reduction in the number of tiny Au particles surrounding the Au disk (Ostwald ripening) as well as transformation of the Au nanoantenna towards a more Wulff-like shape. Predominantly, the changes take place in the Au nanoantenna, in line with the drift essentially being the same for both polarization directions.

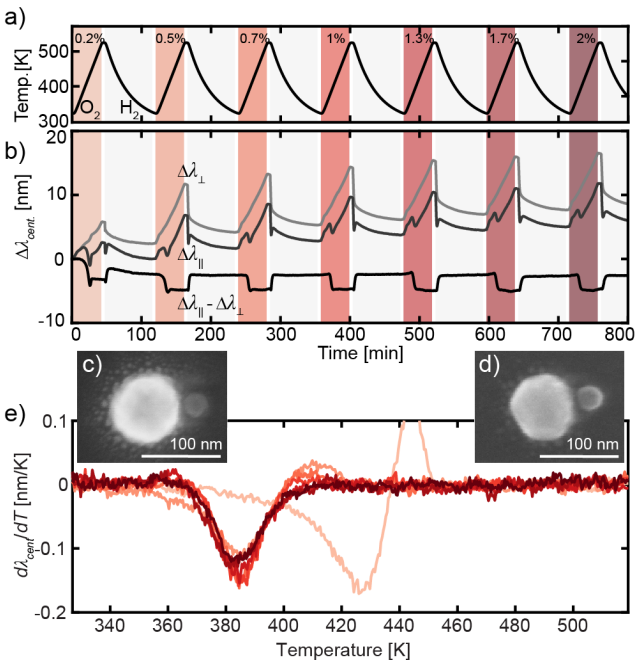

Figure 2 *a) Temperature ramps from 323 K to 523 K in different O_2 concentrations in Ar carrier gas, as indicated by the red shaded areas. The white shaded areas correspond to cooling cycles back to 323 K in 4% H_2 in Ar carrier gas to induce reduction of the Cu nanoparticles. b) Corresponding LSPR centroid position shift, $\Delta\lambda_{cent.}$, of a Au-Cu heterodimer array for light polarized parallel ($\Delta\lambda_{//}$) and perpendicular ($\Delta\lambda_{\perp}$) to the dimer axis, as well as for the difference between the two ($\Delta\lambda_{//} - \Delta\lambda_{\perp}$). Note how the subtraction of the two polarizations effectively eliminates drift, as well as the temperature-induced optical*

response of the dimer. c,d) SEM images of a representative heterodimer taken before and after, respectively, the experimental sequence outlined in (a). e) Time derivative of the drift-corrected $\Delta\lambda_{cent.}$ response plotted as a function of temperature. The color code corresponds to the one in (a) and depicts the O_2 concentration in the feed during the oxidation cycle. While the first oxidation cycle exhibits a distinctly different response with an oxidation temperature of ca. 423 K (defined as the minimum in the derivative), a very similar oxidation behavior with oxidation temperature of ca. 383 K is observed for all other O_2 concentration cycles.

To account for and eliminate these three undesirable contributions to the optical signal, we subtracted the perpendicular polarization trace from the parallel one (**Figure 2b**). In this way, we obtain the plasmonic $\Delta\lambda_{cent.}$ signal stemming from the oxidation/reduction of the Cu nanoparticle. As the key observations from this analysis, we find that (i) the long-term drift has been eliminated from the data and (ii) only a distinct spectral blue shift about one third into the temperature ramp is recorded for each oxidation cycle. Furthermore, inspection of a heterodimer before and after cycling reveals that both Au nanoantenna and Cu nanoparticle are apparently nearly intact (**Figure 2c,d**).

To further analyze these data, we plot the first derivative of the $\Delta\lambda_{cent.}$ signal *versus* temperature[23] (**Figure 2e**). In this way, we can identify the temperature at which oxidation occurs for each O_2 concentration in the gas feed, in analogy to traditional temperature-programmed oxidation. This analysis reveals, apart from the first oxidation cycle, a very similar oxidation behavior for the screened range of different O_2 concentrations. This indicates that (i) our experimental approach is robust, (ii) the Cu nanoparticles are insensitive to O_2 concentration in the range of 0.5 – 2 % and (iii) the very first oxidation is mechanistically distinct from the subsequent ones, as reveled by the significantly higher

oxidation temperature. As a consequence, we have excluded the first oxidation cycle from further analysis below.

Having established our experimental approach, we now turn to a second set of experiments combined with extensive FDTD simulations to investigate in detail and in a quantitative fashion the oxidation process of the Cu nanoparticles. As the first step, we carried out the controlled oxidation of a sample that had been pre-treated with a full oxidation-reduction cycle at 383 K in 0.5% O_2. This temperature is high enough for oxidation to occur at a reasonable time scale and low enough to predominantly form Cu_2O, while suppressing CuO,[9,12,13] as confirmed by XPS analysis [**Figure S2** in the supporting information (SI)] and in agreement with previous studies of Cu nanoparticle oxidation.[14,43] We make the following initial observations from the experimental data. As oxidation proceeds, the LSPR peak for parallel polarization blue shifts and shoulder-like features appear and evolve on the long-wavelength side (**Figure 3a**). Inspecting SEM images (**Figure 3b, c**) of the same sample together with TEM micrographs obtained before and after identical oxidation treatment of a sample-analogue fabricated on a TEM membrane (**Figure 3b, c – insets** and **Figure S1**), reveals the formation of a central Kirkendall void during oxidation and a corresponding increase of the particle size (**Figure S1)**, in good agreement with earlier observations of the NKE.[4,9,14,30]

Turning back to the optical response induced by the oxide shell growth and Kirkendall void formation, we tracked four different peak descriptors as a function of oxidation time, that is, the peak position $\Delta\lambda$, the centroid position, $\Delta\lambda_{cent.}$, according to the definition by Dahlin et al.,[41] the change in peak full-width-at-half-maximum ($\Delta FWHM$) and the change in extinction value at the peak wavelength (ΔExt), all shown in **Figure 3d-g**. The $\Delta\lambda$ time trace obtained after subtraction of the corresponding perpendicular polarization trace nicely reproduces the blue shift identified from the spectra but also reveals a slight red shift before and after the

blue shifting period (**Figure 3d**). The evolution of the centroid time trace is similar but exhibits a period of more pronounced spectral red shift prior to blue shifting (**Figure 3e**). Looking at the time traces of the remaining two peak descriptors *ΔFWHM* and *ΔExt* reveals a significantly different response, where a distinct maximum or minimum, respectively, occurs during the second half of the *Δλ* blue shift period (**Figure 3f, g**).

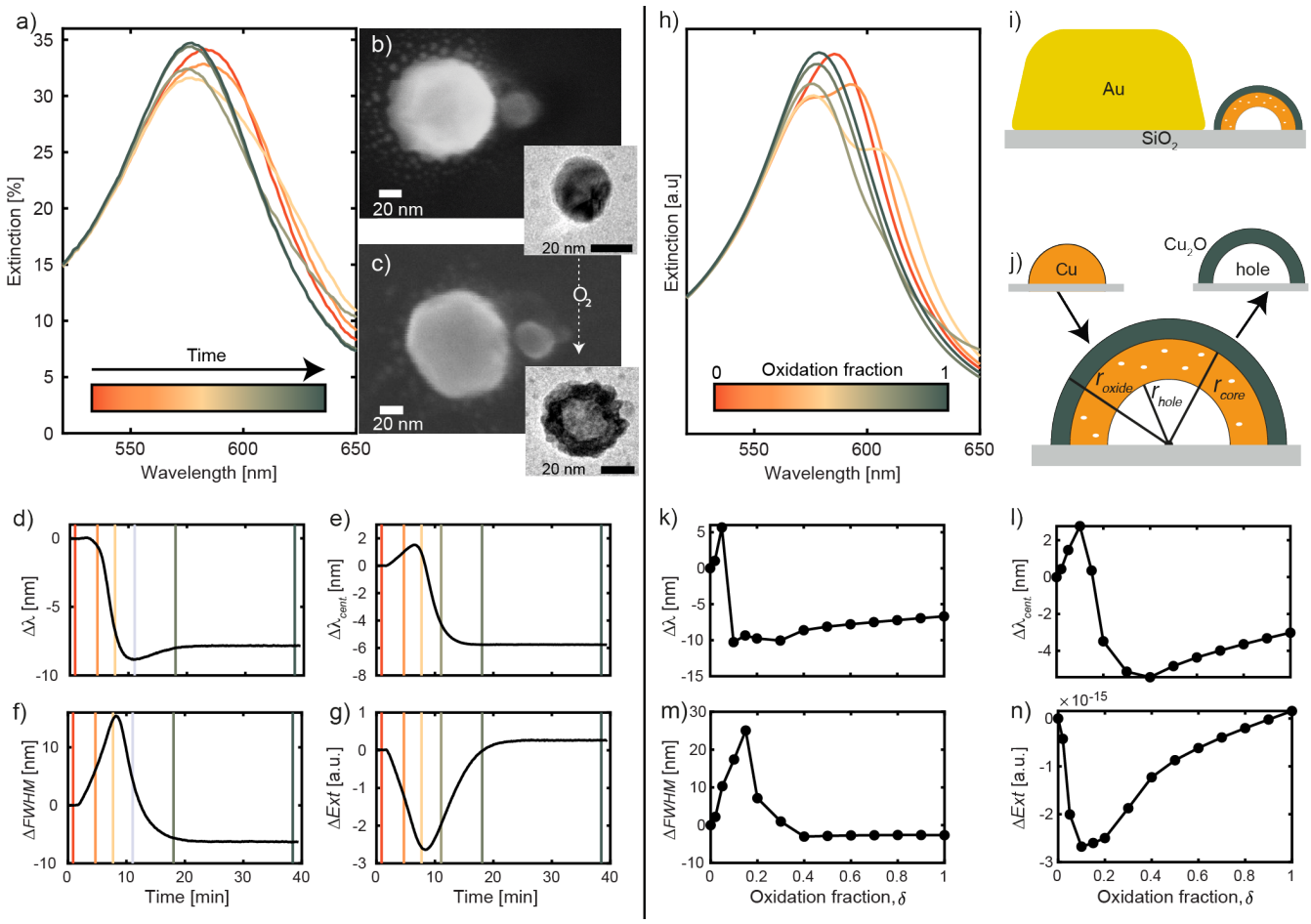

Figure 3. *a) Evolution of the LSPR peak during the oxidation of the Cu elements in an array of Au-Cu heterodimers measured at 383 K in 0.5 % O_2 in Ar carrier gas in parallel polarization configuration. The color code depicts the reaction coordinate between 0 (fully reduced state) to 1 (fully oxidized state). We note the spectral blue shift and the appearance of shoulder-like features on the long-wavelength side of the peak, as oxidation of the Cu*

element progresses. b,c) SEM images of a representative single dimer in the reduced (b) and fully oxidized (c) state. The insets show corresponding TEM images obtained before and after identical oxidation treatment of a sample-analogue fabricated on a TEM membrane. They reveal the formation of a central Kirkendall hole during oxidation. (d-g) Experimentally determined temporal evolution of the four peak descriptors (d) peak position shift, $\Delta\lambda$, (e) peak centroid shift, $\Delta\lambda_{cent.}$ (f) full-width-at-half-maximum change, ΔFWHM, and (g) extinction at peak maximum change, ΔExt. The colored lines indicate the position of the selected spectra shown in (a) along the reaction coordinate. h) Extinction spectra for different degrees of oxidation of the Cu element in a single Au-Cu heterodimer simulated by FDTD for parallel polarization. The color code depicts the volumetric oxidation fraction, δ, of the Cu element. We note the good qualitative agreement with the experimental spectra in (a). i) Schematic depiction of the FDTD model used to simulate the Au-Cu heterodimers. j) Schematic depiction of and geometric descriptors used in the NKE-Cu oxidation model for the corresponding FDTD simulations. k-n) Same as (d-g) but with data taken from the FDTD simulations and plotted versus the oxidation fraction, δ.

FDTD-NKE Model Simulations

The four peak descriptors introduced above allow us to quantify the optical response to oxidation of Cu nanoparticles. However, to actually track the *kinetics* of oxidation, we need a recipe to convert these descriptors into the extent of oxidation. To enable this conversion, we employ electrodynamics simulations of our structures at different stages of oxidation and extract the same peak descriptors from the simulated optical response. Specifically, we utilize the FDTD method due to its capability of simulating the optical response of an arbitrarily shaped nanostructure, including the structures of interest to us. In the FDTD model, the heterodimer structures were represented as a truncated Au cone with rounded corners located

next to a hemispherical Cu particle (**Figure 3i**). Specifically, the Cu particles are described by using a conventional hemispherical core-shell model (**Figure 3j**; for oxidation of Cu, this structural model has been successfully used earlier[9,16]). In particular, the Cu_2O shell of volume V_{oxide} is assumed structurally homogeneous. Due to the NKE, the core volume V_{core} is considered to contain metal and voids. The net volume of metal (without voids) and the volume of voids are designated as V_{Cu} and V_{void}, respectively. For these volumes, we have four general balance equations,

$$V_{Cu} = V_0(1 - \delta) \tag{1}$$

$$V_{void} = V_0\theta\delta \tag{2}$$

$$V_{oxide} = V_0 Z\delta \tag{3}$$

$$V_{core} = V_{Cu} + V_{void} \tag{4}$$

where V_0 is the initial volume of the particle, δ is the fraction of Cu atoms converted into the oxide state, $Z = 1.68$ is the Pilling-Bedworth ratio for Cu_2O formation,[44] and θ is the relative extent of the void formation inside the core compared to its maximum possible value ($\theta \leq 1$).

Physically, $\theta = 0$ corresponds to a situation where only O-ions diffuse inwards and no internal void is formed, while at $\theta = \theta_{max} = 1$ only outward diffusion of Cu-ions occurs and results in the full-scale formation of Kirkendall voids in the core. Since in our case the formation of a central Kirkendall hole and the corresponding increase in particle diameter in the oxide state after complete oxidation are clearly observed, we further focus on the full NKE and thus set $\theta = 1$. With this condition, Eq. (4) is reduced to $V_{core} = V_0$.

The ingredients of the model introduced above are independent of details describing the void distribution in the core. To account for variation in the location and distribution of internal voids we therefore analyzed a few versions of our FDTD model in order to clarify the scale of potential errors related to the uncertainties of the underlying assumptions

(Figures S6 and S7). Here, we describe the version, which appears most reasonable and present the corresponding results.

To specify the description of voids, we notice that in our case, during the initial oxidation phase, a multitude of small voids is expected to form simultaneously inside the metallic phase. We describe them by assuming they form isotopically throughout the metallic phase and grow in number until a critical concentration is reached when they coalesce into a larger void or hole in the center of the nanoparticle. This assumption is reasonable for our particles because they are rich in defects and grain boundaries, as a consequence of the growth conditions during Cu evaporation. This heterogeneity then provides multiple nucleation sites for the initial transient formation of small voids that at the later oxidation stage coalesce into a single large Kirkendall hole.[29] The presence of small voids inside the Cu can be described in terms of their integral volume, V_{sv}, the integral volume of Cu and small voids, $V_{Cu} + V_{sv}$, and the corresponding coefficient of porosity, defined by

$$V_{sv} = \beta(V_{Cu} + V_{sv}). \tag{5}$$

Before the onset of the formation of a large Kirkendall hole, we have $V_{sv} = V_{void} = \delta V_0$. Substituting this expression and expression (1) into (5) yields $\beta = \delta$. In our treatment, we consider that this regime occurs up to reaching the critical value of β (or δ), i.e., at $\beta \leq \beta_* = 0.3$, and then the porosity remains constant (this value of β_* is physically reasonable because at smaller β, large voids are usually not observed[9]). For the later stage of the oxidation, Eq. (5) remains applicable but with $\beta = \beta_*$. In particular, it can be rewritten as $V_{sv} = \left[\frac{\beta_*}{1-\beta_*}\right] V_{Cu} = \left[\frac{\beta_*}{1-\beta_*}\right](1-\delta)V_0$. Using the latter relation and considering that the full volume of pores is δV_0 (see Eq. (2) with $\theta = 1$), we obtain the expression for the hole volume

$$V_{hole} = \delta V_0 - \frac{\beta_*(1-\delta)V_0}{1-\beta_*} = \frac{\delta - \beta_*}{1-\beta_*} V_0. \tag{6}$$

As expected, $V_{hole} = 0$ at $\delta = \beta_*$, and $V_{hole} = V_0$ at $\delta = 1$.

Our FDTD simulations (**Figure 3h,k-n**) were performed for a hemispherical Cu particle (22 nm in diameter) located next to (8 nm gap) a truncated Au cone (81 nm bottom diameter, 66 nm top diameter and 42 nm thickness). These dimensions are slightly different compared to the experimentally measured ones. The difference is a consequence of tuning the simulated spectra to match the resonance wavelength observed experimentally to compensate for the characteristic stochastic intra-array coupling present in our experimental system[45]. This matching is important to ensure that the simulated plasmonic peak "probes" the spectrally appropriate parts of the dispersive refractive indices of Cu/Cu_2O that are the same as in the experiment. The difference is a consequence of tuning the simulated spectra to match the resonance wavelength observed experimentally. The dielectric functions of Cu, Cu with voids, and Cu_2O are presented in the Methods and SI (in particular we used the Maxwell-Garnett approximation for Cu with small voids; at $\beta \leq \beta_* = 0.3$, this approximation is considered fairly accurate[46]).

With the specification above, in good agreement with the experiment (cf. **Figures 3h** and **3a**), an initial spectral red-shift, followed by a larger blue-shift is reproduced in the FDTD-simulated spectra, and shoulder-like features emerge on the long-wavelength side of the peak, indicating that the oxidation mechanism is captured very well by the model. The more distinct nature of the long-wavelength features riding on top of the broad LSPR peak is a consequence of the ensemble averaging in the experiment, compared to the simulation, which is done for a single nanoparticle. The obtained response captures all the key features observed for the different descriptors ($\Delta\lambda$, $\Delta\lambda_{cent.}$, $\Delta FWHM$ and ΔExt) (cf. **Figures 3d-g, k-n**). We also note that simulating the same oxidation process with the incident field polarized perpendicular to the dimer axis results in an essentially constant optical signature, in agreement with the corresponding experimental data (**Figure S4**).

To evaluate the robustness of the results presented above, we also performed the calculations based on three other slightly different versions of the model: (i) locating the Kirkendall hole off-center of the particle to break symmetry (**Figure S5**), (ii) using the Maxwell-Garnett approximation up to 100% void inclusion (**Figure S6c**), and (iii) nucleating the Kirkendall void at a specific position of the metal-oxide interface instead of in the center of the nanoparticle (**Figure S6a**). The corresponding results, presented in **Figure S6**, indicate that the main trends observed experimentally in the evolution of the optical response are qualitatively captured by all the model versions but that the version introduced above describes the experimental observations most accurately, corroborating our choice to rely on it for the further interpretation of the experimentally measured oxidation kinetics.

Cu Oxidation Kinetics

Having established our FDTD-NKE model and benchmarked it with the corresponding experimental data, we can now apply it to in detail quantify the oxidation process. As the first step, we utilize the simulations to assign an oxidation fraction to the experimentally measured temporal evolution of the LSPR peak descriptors. For this purpose, we carried out an experiment where we collected the optical response (using the same four peak descriptors as above) of a heterodimer sample during 8 isothermal oxidation cycles in 0.5 % O_2 in Ar, carried out at temperatures ranging between 363 K and 423 K with 10 K increments, using parallel and perpendicular polarization (**Figure 4a** for experimental sequence and **Figure 4b** for a $\Delta\lambda_{cent.}$ readout example). After each oxidation cycle, we reduced the particles in 2 % H_2 in Ar carrier gas at 493 K. The specific oxidation temperature range was again chosen to favor the formation of Cu_2O over CuO.[9,12,13] The long term drift in the $\Delta\lambda_{||}$ signal, observed in **Figure 4b,** can be ascribed to minor changes of the structure of the Cu nanoparticles after

each completed oxidation-reduction cycle (e.g. due to reshaping of the Cu particle), resulting in a gradual blue shift of the signal.

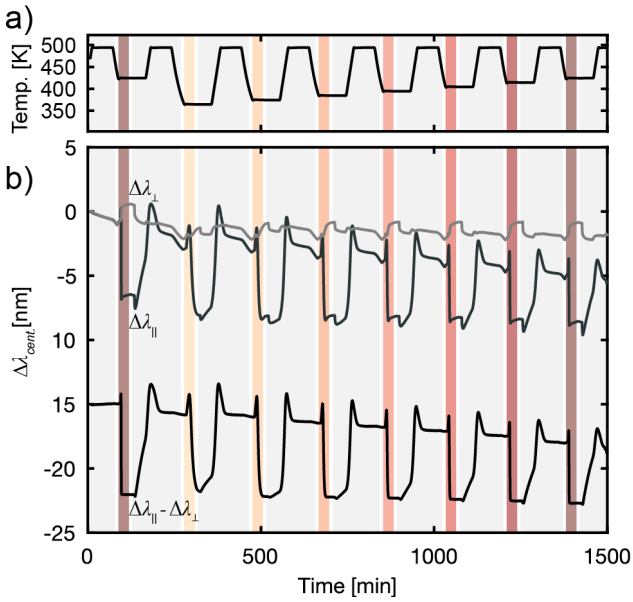

Figure 4. *(a) Schematic depiction of the experimental sequence for the cyclic isothermal oxidation of Cu nanoparticles in 0.5 % O_2 (red shaded areas) in Ar carrier gas, using a different temperature for each cycle. After each oxidation the Cu particles are reduced in 2 % H_2 (gray shaded areas) in Ar carrier gas at 493 K. (b) Corresponding optical, $\Delta\lambda_{cent.}$, response for parallel ($\Delta\lambda_{//}$) and perpendicular ($\Delta\lambda_{\perp}$) polarizations, as well as the latter subtracted from the former. For clarity, the subtracted parallel-perpendicular $\Delta\lambda_{cent.}$ response is offset by -15 nm. The areas shaded in color denote the O_2 exposure pulses at different temperatures and the light-grey shaded areas the reduction cycles in 2 % H_2.*

Similarly extracting the time evolution for all four peak descriptors, and plotting them together for each oxidation cycle temperature, reveals that extreme points (maxima or minima) occur at different times and thus oxidation fractions for the different descriptors

(**Figure 5a-d**). Furthermore, the extreme points occur at different absolute time for the different oxidation temperatures. In a first step to quantify the oxidation process, we can thus use the temperature dependence of these extreme points (presented by symbols in **Figure 5a-d**) to analyze the kinetics of the oxidation process. Specifically, we assume that at each extent of oxidation the time needed to reach this extent can be represented in Arrhenius form,

$$\tau = \tau_0 \exp\left(\frac{E_a}{RT}\right) \tag{7}$$

where τ_0 and E_a are the apparent Arrhenius parameters (i.e. pre-exponential factor and activation energy), R is the gas constant and T is the temperature. By plotting $\ln(\tau_0)$ vs. $1/T$ and then applying a linear fit, we can extract E_a and τ_0 from the slope and the intersection with the y-axis, respectively. The corresponding Arrhenius plots, together with derived apparent activation energies, E_a, for Cu oxidation obtained using the different peak descriptors and their respective used extreme point readouts, are summarized in **Figure 5e-h.** The found values range from 36 to 53.4 kJ/mole, which is at the lower end of the related range of literature values, which spans from 37 kJ/mole to 144 kJ/mole.[9,14]

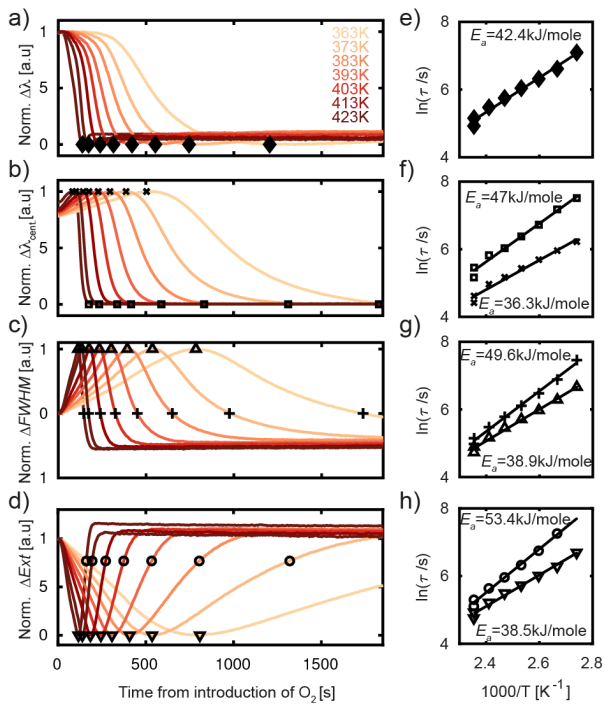

Figure 5. *Time evolution of the extracted peak descriptors: (a) peak position shift, Δλ, (b) centroid shift, $\Delta\lambda_{cent.}$, (c) change in full-width-at-half-maximum, ΔFWHM, and (d) change in extinction at peak maximum, ΔExt, during isothermal oxidation in 0.5% O_2 in Ar at 7 different temperatures ranging from 363 K to 423 K. The symbols (◊,×,□,Δ,+,∇,o) correspond to the tracked extreme points in the respective descriptors' temporal evolution, at which characteristic oxidation times (τ) are extracted for all temperatures. (e-h) Arrhenius plots based on the extracted times (τ) from (a-d) together with the derived apparent activation energies, E_a.*

It is now interesting to analyze if E_a for the different peak descriptors depends on oxidation fraction in a systematic way. For this purpose, we plot the obtained apparent activation energies obtained from the different peak descriptors versus the oxidation fraction, δ, derived from the FDTD simulations for $\delta < 0.4$ (symbols ◊, ×, □, Δ, + in **Figure 6a**). We find that, to a first approximation, all the extracted E_a values follow the same trend when plotted against

the oxidation fraction, δ, which has the following implications. Firstly, it corroborates the robustness of our approach and the interchangeability of the four peak descriptors. This is an interesting result, in particular in view of the quite different qualitative temporal evolution of the respective peak descriptor signal. Secondly, it demonstrates that the apparent activation energy is not constant but dynamically changes as oxidation proceeds. To this end, low activation energies are often attributed to grain boundary diffusion, while higher activation barriers are explained by Cu ion diffusion through an amorphous Cu_2O layer that forms at later oxidation stages and has been found to eliminate grain boundaries.[47] Consequently, it is now interesting to further evaluate the evolution of E_a even in the $\delta > 0.4$ regime all the way to $\delta = 1$, as enabled by our heterodimer sensing approach. For this analysis we employ the *ΔExt* peak descriptor since it exhibits the largest optical contrast at the late oxidation stages. By finding the times at which the *ΔExt* peak descriptor reaches certain values (**Figure S7**), the kinetics of oxidation can be extracted (**Figure 6b**). From this we perform the same Arrhenius analysis as outlined above (**Figure S8**), and as the main result we find that the apparent activation energy exhibits a sizable gradual increase while the pre-exponential factor significantly drops as the oxidation progresses towards completion at $\delta = 1$ (**Figure 6a**). In other words, we observe a significant compensation effect.

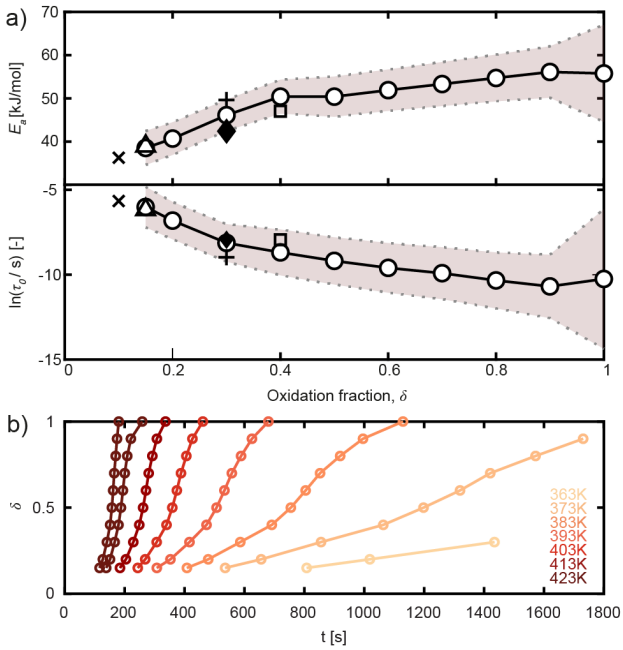

Figure 6. *Kinetics of Cu oxidation. a) Arrhenius parameters E_a and ln(τ_0) for oxidation of the Cu nanoparticles plotted as a function of oxidation fraction, δ, derived from FDTD simulations. The open circles correspond to data points extracted by using the ΔExt peak descriptor (see* ***Figure S8*** *for the corresponding Arrhenius plots) and the shaded areas depict the corresponding 95% confidence bounds of the Arrhenius fit. The additional symbols (◊,×,□,Δ,+) correspond to the E_a values derived and presented in* ***Figure 5 e-h*** *using the other three peak descriptors. b) Oxidation fraction, δ, as a function of time for the different considered temperatures.*

To illustrate the extent of compensation, we show τ as a function of δ at the average temperature $\langle T \rangle$ = 393 K (**Figure 7a**) and the normalized change of the apparent activation energies together with the corresponding normalized pre-exponential factors also as a function of δ (**Figure 7b**). The observed compensation between the two Arrhenius parameters can mathematically be expressed as

$$\ln(\tau_0) = k + mE_a, \tag{8}$$

where k and m are constants (inset of **Figure 7b**). In our case, $m \simeq -0.26$ 1/(kJ/mole) which is comparable to $\frac{1}{R\langle T\rangle}$, indicating that the extent of compensation is significant.

To articulate the difference between what we observe and what one might expect to see on the basis of conventional models of oxidation, we consider the simplest core-shell model of oxidation with diffusion of metal ions through the oxide shell and void formation in the core. In such a case, the growth of the oxide layer thickness can be described as $\frac{dl}{dt} \simeq \frac{AD}{l}$ or $l^2 \propto Dt$, where D is the diffusion coefficient, l is the oxide layer thickness and A is a constant. The extent of oxidation, δ, can be considered approximately proportional to l, and thus the time corresponding to a given δ is given by

$$\tau \propto \frac{\delta^2}{D} \propto \delta^2 \exp\left(\frac{E_d}{k_B T}\right) \tag{9}$$

where E_d is the activation energy for diffusion. In this case, the activation energy for oxidation is *independent* of δ and coincides with E_d, while τ_0 increases with increasing δ as $\tau_0 \propto \delta^2$, which is the opposite of what we observe. Thus, the kinetics we experimentally measure indicate a different and most likely more complex oxidation mechanism.

Historically, this type of compensation effect has been observed most prominently in heterogeneous catalysis at the level of complex reactions[48–50] and also at the level of the dependence of the Arrhenius parameters of elementary reaction steps on coverage.[51] Usually, this effect is attributed to a change of the reaction mechanism with increasing temperature or to systematic errors in measurements and/or interpretation[52] (the latter might be the case if the interpretation includes a specific kinetic model which does not correspond to reality). In our case, the systematic errors might be related to the FDTD-NKE model simulations. The scale of this error is, however, only about ± 5 kJ/mole, as estimated by using different versions of our model (see corresponding section in the SI and **Figure S7**) and it is small compared to the observed amount of compensation. Hence, it does not influence our

conclusion and a change of the reaction mechanism with increasing oxidation fraction appears to be the more likely cause of the observed change in apparent Arrhenius parameters. For example, at low extents of oxidation, the oxide layer is thin and oxidation can occur via the Caberra-Mott mechanism, where strong electric fields at the metal-oxide interface can reduce the measured activation energy. Additionally, the low E_a at the early oxidation stage can be a result of many small, disordered grains forming in the oxide as a consequence of the local oxide phase nucleation process on the surface of the metal. As the oxidation progresses, the size of the oxide grains near the metal-oxide interface increases due to recrystallization, and as a consequence, the effective activation energy for diffusion jumps also increases since low energy diffusion sites at grain boundaries become less abundant, giving rise to the experimentally observed increase in the activation energy.

The explanation of the decrease of τ_0 with oxidation extent is less obvious. One of the physically reasonable conjectures here is that this is also related to the grain growth upon progression of oxidation. As already noted, the grains near the oxide-metal interface are expected to be small and highly disordered in the beginning, as a consequence of oxide phase nucleation. Under such conditions, the activation energy for diffusion steps near this interface is distributed over a wide range, and the apparent activation for oxidation is determined by the diffusion steps with the lowest activation energy. The absolute number of available pathways for such steps is, however, low, and accordingly τ_0 is large in this case. With increasing extent of oxidation, the grains formed near the oxide-metal interface grow, the distribution of the activation energy of diffusion steps narrows, the number of accessible pathways for the steps determining the oxidation rate becomes high, and accordingly τ_0 is smaller in this case, explaining the corresponding trend found in our experiments, as well as the found compensation effect of the Arrhenius parameters.

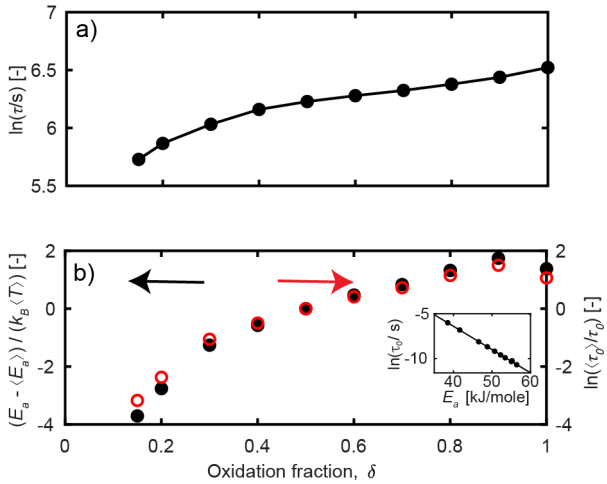

Figure 7. *Kinetic parameters for Cu oxidation. a) Characteristic times (τ) at different levels of oxidation, δ, extracted at the average experimental temperature $\langle T \rangle$ = 393 K. b) Normalized change in activation energy, $E_a - \langle E_a \rangle$ (where $\langle E_a \rangle$ is the value of E_a at δ = 0.5), and logarithm of the pre-exponential factors, $\ln \frac{\langle \tau_0 \rangle}{\tau_0}$, as a function of δ. The inset shows $\ln(\tau_0)$ as function of E_a in order to illustrate the linear relationship between the Arrhenius parameters [Eq. (9) with $m \simeq -0.26$ 1/(kJ/mole)].*

Conclusion

In summary, we have presented a method to experimentally investigate metal nanoparticle oxidation *in situ* by means of plasmonic optical spectroscopy. It employs a plasmonic heterodimer nanoarchitecture, which enables continuous self-referencing using polarized light to eliminate parasitic signals and to provide large optical contrast all the way to complete oxidation. Using this approach in combination with detailed FDTD electrodynamics

simulations explicitly taking into account the Kirkendall void formation observed by *ex situ* TEM analysis, we have been able to quantitatively analyze the oxidation kinetics of ca. 30 nm sized Cu nanoparticles all the way to complete oxidation. We found a distinct dependence of the corresponding Arrhenius parameters (E_a and τ_0) on the extent of oxidation with, as the general trend, increasing apparent activation energy E_a for progressing oxidation, and for the initial oxidation stages, absolute values in good agreement with the available literature. Additionally, we observed a significant kinetic compensation effect where the pre-exponential factor (τ_0) decreases as the apparent activation energy (E_a) increases during progressing oxidation. We attribute these sizable changes in the Arrhenius parameters to changes in the oxidation mechanism mainly dictated by the evolution of the grain structure in the growing oxide, emphasizing the complex nature of oxidation processes in nanoparticles. In a wider perspective, our work demonstrates the usefulness of combining experiments, based on nanoarchitectures tailored for *in situ* optical plasmonic spectroscopy, with mechanistic FDTD electrodynamics simulations, as a tool to quantitatively analyze and mechanistically interpret oxidation processes of metal nanoparticles and the corresponding kinetics. Hence it also opens the door to non-invasive *in situ* investigations of metal nanoparticle oxidation during, for example, a catalytic reaction or in a corrosive environment.

ASSOCIATED CONTENT

Supporting Information.

SI file – TEM images of Cu nanoparticles, XPS characterization, dielectric function calculations of porous Cu, polarization dependent FDTD simulations, Arrhenius fit from optical data and alternative FDTD models.

Corresponding Author

*clangham@chalmers.se.

Author Contributions

The manuscript was written through contributions of all authors. All authors have given approval to the final version of the manuscript.

ACKNOWLEDGMENTS

This research has received funding from the European Research Council (ERC) under the European Union's Horizon 2020 research and innovation programme (678941/SINCAT) and from the Knut and Alice Wallenberg Foundation project 2015.0055. We also thank the Knut and Alice Wallenberg Foundation for their support of the infrastructure in the MC2 nanofabrication laboratory at Chalmers. V.P.Zh. thanks the support of Russian Academy of Sciences and Federal Agency for Scientific Organizations (project 0303-2016-0001). This work was in part performed at the Chalmers Materials Analysis Laboratory, CMAL.

REFERENCES

(1) Hauffe, K. *Oxidation of Metals*; Springer US: Boston, MA, 1995.

(2) Yin, Y.; Rioux, R. M.; Erdonmez, C. K.; Hughes, S.; Somorjai, G. A.; Alivisatos, A. P. Formation of Hollow Nanocrystals through the Nanoscale Kirkendall Effect. *Science* **2004**, *304*, 711–714.

(3) Chen, C. H.; Yamaguchi, T.; Sugawara, K. I.; Koga, K. Role of Stress in the Self-Limiting Oxidation of Copper Nanoparticles. *J. Phys. Chem. B* **2005**, *109*, 20669–20672.

(4) Nakamura, R.; Tokozakura, D.; Nakajima, H.; Lee, J.-G.; Mori, H. Hollow Oxide Formation by Oxidation of Al and Cu Nanoparticles. *J. Appl. Phys.* **2007**, *101*, 074303.

(5) Sutter, E.; Sutter, P. Size-Dependent Room Temperature Oxidation of In Nanoparticles. *J. Phys. Chem. C* **2012**, *116*, 20574–20578.

(6) Wang, W.; Dahl, M.; Yin, Y. Hollow Nanocrystals through the Nanoscale Kirkendall Effect. *Chem. Mater.* **2013**, *25*, 1179–1189.

(7) Han, L.; Meng, Q.; Wang, D.; Zhu, Y.; Wang, J.; Du, X.; Stach, E. A.; Xin, H. L. Interrogation of Bimetallic Particle Oxidation in Three Dimensions at the Nanoscale. *Nat. Commun.* **2016**,

7, 13335.

(8) Lagrow, A. P.; Ward, M. R.; Lloyd, D. C.; Gai, P. L.; Boyes, E. D. Visualizing the Cu/Cu2O Interface Transition in Nanoparticles with Environmental Scanning Transmission Electron Microscopy. *J. Am. Chem. Soc.* **2017**, *139*, 179–185.

(9) Susman, M. D.; Feldman, Y.; Bendikov, T. A.; Vaskevich, A.; Rubinstein, I. Real-Time Plasmon Spectroscopy Study of the Solid-State Oxidation and Kirkendall Void Formation in Copper Nanoparticles. *Nanoscale* **2017**, *9*, 12573–12589.

(10) Zhdanov, V. P. Oxidation of Metal Nanoparticles with the Grain Growth in the Oxide. *Chem. Phys. Lett.* **2017**, *674*, 136–140.

(11) Pedersen, D. B.; Wang, S.; Liang, S. H. Charge-Transfer-Driven Diffusion Processes in Cu@Cu-Oxide Core−Shell Nanoparticles: Oxidation of 3.0 ± 0.3 Nm Diameter Copper Nanoparticles. *J. Phys. Chem. C* **2008**, *112*, 8819–8826.

(12) Yabuki, A.; Tanaka, S. Oxidation Behavior of Copper Nanoparticles at Low Temperature. *Mater. Res. Bull.* **2011**, *46*, 2323–2327.

(13) Mansour, M.; Favergeon, L.; Pijolat, M. Kinetic Modeling of Low Temperature Oxidation of Copper Nanoparticles by O2. *Thermochim. Acta* **2013**, *570*, 41–50.

(14) Rice, K. P.; Paterson, A. S.; Stoykovich, M. P. Nanoscale Kirkendall Effect and Oxidation Kinetics in Copper Nanocrystals Characterized by Real-Time, in Situ Optical Spectroscopy. *Part. Part. Syst. Charact.* **2015**, *32*, 373–380.

(15) Cure, J.; Glaria, A.; Collière, V.; Fazzini, P.-F.; Mlayah, A.; Chaudret, B.; Fau, P. Remarkable Decrease in the Oxidation Rate of Cu Nanocrystals Controlled by Alkylamine Ligands. *J. Phys. Chem. C* **2017**, *121*, 5253–5260.

(16) Susman, M. D.; Vaskevich, A.; Rubinstein, I. A General Kinetic-Optical Model for Solid-State Reactions Involving the Nano Kirkendall Effect. The Case of Copper Nanoparticle Oxidation. *J. Phys. Chem. C* **2016**, *120*, 16140–16152.

(17) Tokozakura, D.; Nakamura, R.; Nakajima, H.; Lee, J.-G.; Mori, H. Transmission Electron Microscopy Observation of Oxide Layer Growth on Cu Nanoparticles and Formation Process of Hollow Oxide Particles. *J. Mater. Res.* **2007**, *22*, 2930–2935.

(18) Zhang, D.; Jin, C.; Li, Z. Y.; Zhang, Z.; Li, J. Oxidation Behavior of Cobalt Nanoparticles Studied by in Situ Environmental Transmission Electron Microscopy. *Sci. Bull.* **2017**, *62*, 775–778.

(19) Yeshchenko, O. A.; Bondarchuk, I. S.; Gurin, V. S.; Dmitruk, I. M.; Kotko, A. V. Temperature Dependence of the Surface Plasmon Resonance in Gold Nanoparticles. *Surf. Sci.* **2013**, *608*, 275–281.

(20) Wettergren, K.; Hellman, A.; Cavalca, F.; Zhdanov, V. P.; Langhammer, C. Unravelling the Dependence of Hydrogen Oxidation Kinetics on the Size of Pt Nanoparticles by in Operando Nanoplasmonic Temperature Sensing. *Nano Lett.* **2015**, *15*, 574–580.

(21) Ghodselahi, T.; Zahrabi, H.; Saani, M. H.; Vesaghi, M. A. CO Gas Sensor Properties of Cu@CuO Core–Shell Nanoparticles Based on Localized Surface Plasmon Resonance. *J. Phys. Chem. C* **2011**, *115*, 22126–22130.

(22) Wallin, M.; Grönbeck, H.; Spetz, A. L.; Eriksson, M.; Skoglundh, M. Vibrational Analysis of H2 and D2 Adsorption on Pt/SiO2. *J. Phys. Chem. B* **2005**, *109*, 9581–9588.

(23) Wadell, C.; Langhammer, C. Drift-Corrected Nanoplasmonic Hydrogen Sensing by Polarization. *Nanoscale* **2015**, *7*, 10963–10969.

(24) Chan, G. H.; Zhao, J.; Hicks, E. M.; Schatz, G. C.; Van Duyne, R. P. Plasmonic Properties of Copper Nanoparticles Fabricated by Nanosphere Lithography. *Nano Lett.* **2007**, *7*, 1947–1952.

(25) Fujita, K.; Ando, D.; Uchikoshi, M.; Mimura, K.; Isshiki, M. New Model for Low-Temperature Oxidation of Copper Single Crystal. *Appl. Surf. Sci.* **2013**, *276*, 347–358.

(26) Kusano, K. F.; Uchikoshi, M.; Mimura, K.; Isshiki, M. Low-Temperature Oxidation of Cu(100), Cu(110) and Cu(111). *Oxid. Met.* **2014**, *82*, 181–193.

(27) Fan, H. J.; Gösele, U.; Zacharias, M. Formation of Nanotubes and Hollow Nanoparticles Based on Kirkendall and Diffusion Processes: A Review. *Small* **2007**, *3*, 1660–1671.

(28) Yang, Z.; Yang, N.; Pileni, M.-P. Nano Kirkendall Effect Related to Nanocrystallinity of Metal Nanocrystals: Influence of the Outward and Inward Atomic Diffusion on the Final Nanoparticle Structure. *J. Phys. Chem. C* **2015**, *119*, 22249–22260.

(29) El Mel, A.-A.; Buffière, M.; Tessier, P.-Y.; Konstantinidis, S.; Xu, W.; Du, K.; Wathuthanthri, I.; Choi, C.-H.; Bittencourt, C.; Snyders, R. Highly Ordered Hollow Oxide Nanostructures: The Kirkendall Effect at the Nanoscale. *Small* **2013**, *9*, 2838–2843.

(30) Watanabe, Y.; Mowbray, R. W.; Rice, K. P.; Stoykovich, M. P. Kinetic Description of Metal Nanocrystal Oxidation: A Combined Theoretical and Experimental Approach for Determining Morphology and Diffusion Parameters in Hollow Nanoparticles by the Nanoscale Kirkendall Effect. *Philos. Mag.* **2014**, *94*, 3487–3506.

(31) Johnson, P. B.; Christy, R. W. Optical Constants of the Noble Metals. *Phys. Rev. B* **1972**, *6*, 4370–4379.

(32) McPeak, K. M.; Jayanti, S. V.; Kress, S. J. P.; Meyer, S.; Iotti, S.; Rossinelli, A.; Norris, D. J. Plasmonic Films Can Easily Be Better: Rules and Recipes. *ACS Photonics* **2015**, *2*, 326–333.

(33) Tahir, D.; Tougaard, S. Electronic and Optical Properties of Cu, CuO and Cu2O Studied by Electron Spectroscopy. *J. Phys. Condens. Matter* **2012**, *24*, 175002.

(34) Fredriksson, H.; Alaverdyan, Y.; Dmitriev, A.; Langhammer, C.; Sutherland, D. S.; Zäch, M.; Kasemo, B. Hole-Mask Colloidal Lithography. *Adv. Mater.* **2007**, *19*, 4297–4302.

(35) Syrenova, S.; Wadell, C.; Langhammer, C. Shrinking-Hole Colloidal Lithography: Self-Aligned Nanofabrication of Complex Plasmonic Nanoantennas. *Nano Lett.* **2014**, *14*, 2655–2663.

(36) Gunnarsson, L.; Rindzevicius, T.; Prikulis, J.; Kasemo, B.; Käll, M.; Zou, S.; Schatz, G. C. Confined Plasmons in Nanofabricated Single Silver Particle Pairs: Experimental Observations of Strong Interparticle Interactions. *J. Phys. Chem. B* **2005**, *109*, 1079–1087.

(37) Hammer, B.; Norskov, J. K. Why Gold Is the Noblest of All the Metals. *Nature* **1995**, *376*, 238–240.

(38) Prodan, E.; Radloff, C.; Halas, N. J.; Nordlander, P. A Hybridization Model for the Plasmon Response of Complex Nanostructures. *Science* **2003**, *302*, 419–422.

(39) Nordlander, P.; Oubre, C.; Prodan, E.; Li, K.; Stockman, M. I. Plasmon Hybridization in Nanoparticle Dimers. *Nano Lett.* **2004**, *4*, 899–903.

(40) Alekseeva, S.; Fanta, A. B. da S.; Iandolo, B.; Antosiewicz, T. J.; Nugroho, F. A. A.; Wagner, J. B.; Burrows, A.; Zhdanov, V. P.; Langhammer, C. Grain Boundary Mediated Hydriding Phase Transformations in Individual Polycrystalline Metal Nanoparticles. *Nat. Commun.* **2017**, *8*, 1084.

(41) Dahlin, A. B.; Tegenfeldt, J. O.; Höök, F. Improving the Instrumental Resolution of Sensors Based on Localized Surface Plasmon Resonance. *Anal. Chem.* **2006**, *78*, 4416–4423.

(42) Ringe, E.; Van Duyne, R. P.; Marks, L. D. Wulff Construction for Alloy Nanoparticles. *Nano Lett.* **2011**, *11*, 3399–3403.

(43) Yin, M.; Wu, C.-K.; Lou, Y.; Burda, C.; Koberstein, J. T.; Zhu, Y.; O'Brien, S. Copper Oxide Nanocrystals. *J. Am. Chem. Soc.* **2005**, *127*, 9506–9511.

(44) *CRC Handbook of Chemistry and Physics, 99th Edition (Internet Version 2018)*; Rumble, J. R., Ed.; CRC Press/Taylor & Francis: Boca Raton, FL, 2018.

(45) Antosiewicz, T. J.; Apell, S. P.; Zäch, M.; Zorić, I.; Langhammer, C. Oscillatory Optical Response of an Amorphous Two-Dimensional Array of Gold Nanoparticles. *Phys. Rev. Lett.* **2012**, *109*, 247401.

(46) Niklasson, G. A.; Granqvist, C. G.; Hunderi, O. Effective Medium Models for the Optical Properties of Inhomogeneous Materials. *Appl. Opt.* **1981**, *20*, 26.

(47) Khoviv, A. M.; Nazarenko, I. N.; Churikov, A. A. An Ellipsometric Study of the Oxidation of Thin Copper Films in Oxygen. *Inorg. Mater.* **2001**, *37*, 473–475.

(48) Bond, G. C.; Keane, M. A.; Kral, H.; Lercher, J. A. Compensation Phenomena in Heterogeneous Catalysis: General Principles and a Possible Explanation. *Catal. Rev. - Sci. Eng.* **2000**, *42*, 323–383.

(49) L'vov, B. V.; Galwey, A. K. Interpretation of the Kinetic Compensation Effect in Heterogeneous Reactions: Thermochemical Approach. *Int. Rev. Phys. Chem.* **2013**, *32*, 515–557.

(50) Liu, L.; Guo, Q.-X. Isokinetic Relationship, Isoequilibrium Relationship, and Enthalpy−Entropy Compensation. *Chem. Rev.* **2001**, *101*, 673–696.

(51) Zhdanov, V. P. Arrhenius Parameters for Rate Processes on Solid Surfaces. *Surf. Sci. Rep.* **1991**, *12*, 185–242.

(52) Barrie, P. J. The Mathematical Origins of the Kinetic Compensation Effect: 1. the Effect of Random Experimental Errors. *Phys. Chem. Chem. Phys.* **2012**, *14*, 318–326.

TOC Graphic